DOI: 10.1021/acsami.0c17575

In Vivo Evaluation of Multifunctional Gold Nanorods for Boron Neutron Capture and Photothermal Therapies

Krishna R. Pulagam,[a] Malou Henriksen-Lacey,[a,b] Kepa B. Uribe,[a] Carlos Renero-Lecuna,[a] Jatish Kumar,[c] Alexandra Charalampopoulou,[d] Angelica Facoetti,[d] Nicoletta Protti,[e,f] Vanessa Gómez-Vallejo,[a] Zuriñe Baz,[a] Vished Kumar,[a] Ana Sánchez-Iglesias,[a,b] Saverio Altieri,[e,f] Unai Cossío,[a] Desire Di Silvio,[a] Angel M. Martínez-Villacorta,[a] Ane Ruiz-de-Angulo,[g] Luka Rejc,[a,h] Luis M. Liz-Marzán,[a,b,i] and Jordi Llop[a,j]*

[a] CIC biomaGUNE, Basque Research and Technology Alliance (BRTA), Paseo de Miramón 194, 20014 Donostia-San Sebastian, Spain.

[b] Centro de Investigación Biomédica en Red de Bioingeniería, Biomateriales y Nanomedicina (CIBER-BBN), Paseo de Miramón 194, 20014 Donostia-San Sebastian, Spain

[c] Department of Chemistry, Indian Institute of Science Education and Research (IISER) Tirupati, Tirupati 517507, India.

[d] Research and Development Department, CNAO National Center for Oncological Hadrontherapy, Pavia, Italy.

[e] Department of Physics, University of Pavia, 27100 Pavia, Italy.

[f] National Institute of Nuclear Physics, Pavia Section, 27100 Pavia, Italy.

[g] CIC bioGUNE, Basque Research and Technology Alliance (BRTA), Bizkaia Science & Technology Park bld 801 A, 48160 Derio, Bizkaia, Spain.

[h] University of Ljubljana, Faculty of Chemistry and Chemical Technology, Večna pot 113, Ljubljana, Slovenia.

[i] Ikerbasque, Basque Foundation for Science, 48013 Bilbao, Spain.

[j] Centro de Investigación Biomédica en Red de Enfermedades Respiratorias (CIBERES), 28029 Madrid, Spain.

[*] e-mail: jllop@cicbiomagune.es; Phone number: +34 943 005 333

KEYWORDS.

Gold Nanorods, Boron Neutron Capture Therapy, Photothermal Therapy, Positron Emission Tomography.

ABSTRACT

The incidence and mortality of cancer demand more innovative approaches and combination therapies to increase treatment efficacy and decrease off-target side effects. We describe a boron-rich nanoparticle composite with potential applications in both boron neutron capture therapy (BNCT) and photothermal therapy (PTT). Our strategy is based on gold nanorods (AuNRs) stabilized with polyethylene glycol and functionalized with the water-soluble complex cobalt *bis*(dicarbollide) ([3,3'-Co(1,2-$C_2B_9H_{11})_2$]$^-$), commonly known as COSAN. Radiolabeling with the positron emitter copper-64 (^{64}Cu) enabled *in vivo* tracking using positron emission tomography (PET) imaging. ^{64}Cu-labeled multifunctionalized AuNRs

proved radiochemically stable and capable to accumulate in the tumor after intravenous administration in a mouse xenograft model of gastrointestinal cancer. The resulting multifunctional AuNRs showed high biocompatibility and the capacity to induce local heating under external stimulation and trigger cell death in heterogeneous cancer spheroids, as well as the capacity to decrease cell viability under neutron irradiation in cancer cells. These results position our nanoconjugates as suitable candidates for combined BNCT/PTT therapies.

INTRODUCTION

Boron neutron capture therapy (BNCT) is a binary approach to treat cancer, based on the ability of boron-10 (^{10}B) to capture thermal neutrons, subsequently instigating a ^{10}B(n, α, γ)^{7}Li nuclear reaction.[1] The resulting alpha particles and ^{7}Li recoil ions have high linear energy transfer and average path lengths in the range of a single cell diameter. Internalization of ^{10}B and irradiation with neutrons therefore causes cellular damage and triggers cell death. To ensure the success of BNCT cancer treatment, selective uptake of a sufficient amount of ^{10}B by cancer cells and a neutron beam of appropriate intensity are required. Under such conditions, thermal neutron irradiation would lead to cancer cell death, while sparing healthy surrounding tissue.

Successful application of BNCT in the clinical arena has been thwarted by a number of difficulties. One of them is the unease around conducting clinical irradiations in nuclear research reactors, which has been recently mitigated by the installation of hospital-based accelerators delivering high intensity epithermal neutron beams.[2-3] Another major limitation is the need for the development of BNCT drugs capable to selectively (or preferentially) accumulate boron atoms in tumor cells and tissues. Different molecular modalities have been proposed as BNCT drug candidates, including boronated carbohydrates, amino acids, peptides, nucleic acids, and immunoconjugates.[4-5] However, and in spite of huge efforts, only

two compounds, namely sodium borocaptate (BSH) and *p*-boronophenylalanine (BPA), are currently approved for clinical trials.[6] Still, they do not show sufficiently high specificity and offer good results only in certain tumor types.[7]

The recent emergence of nanotechnology has opened new opportunities to achieve preferential delivery of large amounts of boron atoms into tumors, by taking advantage of the enhanced permeability and retention (EPR) effect.[8] Such an effect results from the presence of leaky vasculature and deficient lymphatic drainage in the vicinity of tumors, which ultimately results in a passive accumulation of non-targeted nanosized materials in tumor tissue after intravenous administration. A plethora of nanostructured materials that rely on the EPR effect have been proposed as boron delivery agents, including liposomes,[9-13] carbon nanotubes,[14] boron nitride nanotubes,[15-18] magnetic nanoparticles,[19-20] boron carbide nanoparticles,[21-22] borosilicates,[23] gold nanoparticles,[24-25] and carbon dots.[26] Noteworthy, the EPR effect is a highly heterogeneous phenomenon, which varies substantially among different tumor types, patients and even regions within a single tumor.[27-28] As a consequence, the extravasation of boron-rich nanomedicines may follow a heterogeneous pattern and lead to suboptimal treatment efficacy, due to the short range of recoil ions generated upon neutron irradiation. Additionally, the accumulation of boron in the tumor is often insufficient to guarantee therapeutic efficacy. This limitation could be overcome by developing boron carriers that enable the combination of two different therapeutic approaches, *e.g.* BNCT and photothermal therapy (PTT). PTT relies on the administration of photoabsorbers, which, after accumulation in the target tissue, release energy derived from light absorption as heat, thereby inducing thermal damage to surrounding tumor cells.

Herein, we report on the preparation, characterization and *in vivo* application of gold nanorods (AuNRs) grafted with poly(ethylene glycol) methyl ether thiol (mPEG), and COSAN, an inorganic, boron-based anion, cobalt *bis*(dicarbollide) ([3,3'-Co(1,2-$C_2B_9H_{11})_2]^-$)

(Figure 1). Radiolabeling with the positron emitter copper-64 (^{64}Cu) followed by *in vivo* Positron Emission Tomography (PET) imaging of radiolabeled AuNRs in a mouse cancer model were performed, together with complementary *ex vivo* techniques, to confirm accumulation of the nanoconjugates in tumor tissue. *In vitro* studies further demonstrated the capacity of the newly developed nanoconjugates to induce cell damage under near infrared (NIR) light irradiation, thus enabling PTT. Significant accumulation in tumor tissue, together with a high density of boron atoms at the AuNRs surface, and the demonstrated ability of our AuNRs to induce (i) local temperature increase under NIR light irradiation[29-30] and (ii) cell death under neutron irradiation, pave the way towards the development of combined BNCT/PTT therapies.

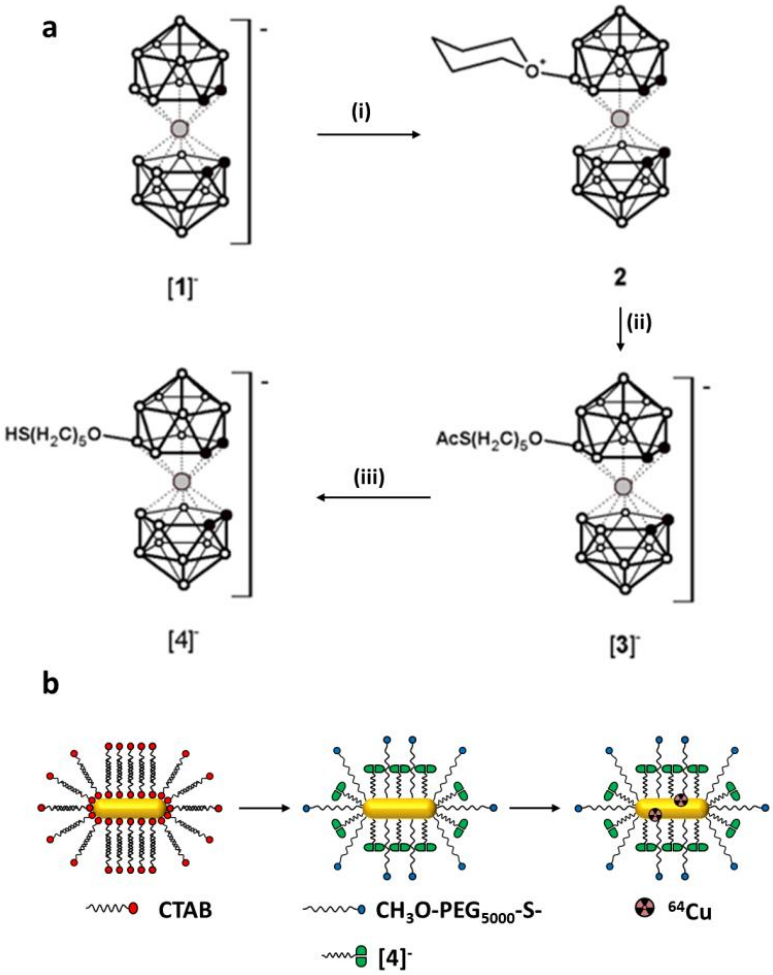

Figure 1: a) Reaction scheme for the synthesis of thiolated cobalt *bis*(dicarbollide) derivatives: (i) tetrahydropyran (THP), dimethylsulphate, H_2SO_4; (ii) KSAc; (iii) NaOMe, MeOH. b) Schematic representation of the synthesis of functionalized AuNRs (AuNR-mPEG@**[4]**$^-$)). The final step comprises radiolabeling with ^{64}Cu to enable *in vivo* PET imaging.

RESULTS AND DISCUSSION

Synthesis and Characterization of PEG–COSAN-AuNR

The synthesis of [3,3']-Co(8-SH-$(CH_2)_5$-O-1,2-$C_2B_9H_{10}$)(1',2'-$C_2B_9H_{11}$)]$^-$ **([4]$^-$)** was designed to introduce a thiol group-bearing COSAN derivative, and thereby facilitate binding onto AuNRs (Figure 1a). Compound **2** ([3,3'-Co(8-C_5H_{10}O-1,2-$C_2B_9H_{10}$)(1',2'-$C_2B_9H_{11}$)]),[31] was therefore treated with potassium thioacetate (KSAc) to yield **[3]**$^-$, which, after basic hydrolysis, led to compound **[4]**$^-$ in an overall yield of 45%. All intermediates and the final product were characterized by ^{1}H-, ^{11}B-, and ^{13}C-NMR.

CTAB-stabilized AuNRs (AuNR-CTAB) were prepared following a previously reported seedless method.[32] We obtained AuNR-CTAB with average dimensions of 37±3 × 10±1 nm (length × width; aspect ratio 3.7) (Figure 2a) and a longitudinal surface plasmon resonance (SPR) band centered at 811 nm (Figure 2c). A ζ-potential of +35±1 mV was recorded for AuNR-CTAB, due to the positively charged surfactant bilayer (Figure 2d).[33]

To ensure colloidal stability *in vivo* and to enhance biocompatibility and circulation time,[34-35] AuNR-CTAB were modified by replacing surfactant molecules with poly(ethylene glycol) methyl ether thiol (mPEG). Upon mixing AuNR-CTAB with 5 kDa mPEG and stirring for 24 h at room temperature, PEG-stabilized AuNRs (AuNR-mPEG) were obtained, which exhibited a bathochromic shift in the longitudinal SPR band to 819 nm (Figure 2c) but preserved the original size and aspect ratio (Figure 2a, SI Figure S1). The minor shift of the

UV-Vis-NIR extinction maximum confirms the retention of structural and optical properties of the AuNRs after modification. Replacement of positively charged CTAB with neutral PEG chains resulted in ζ-potential values close to neutral (+8±2 mV; Figure 2d).

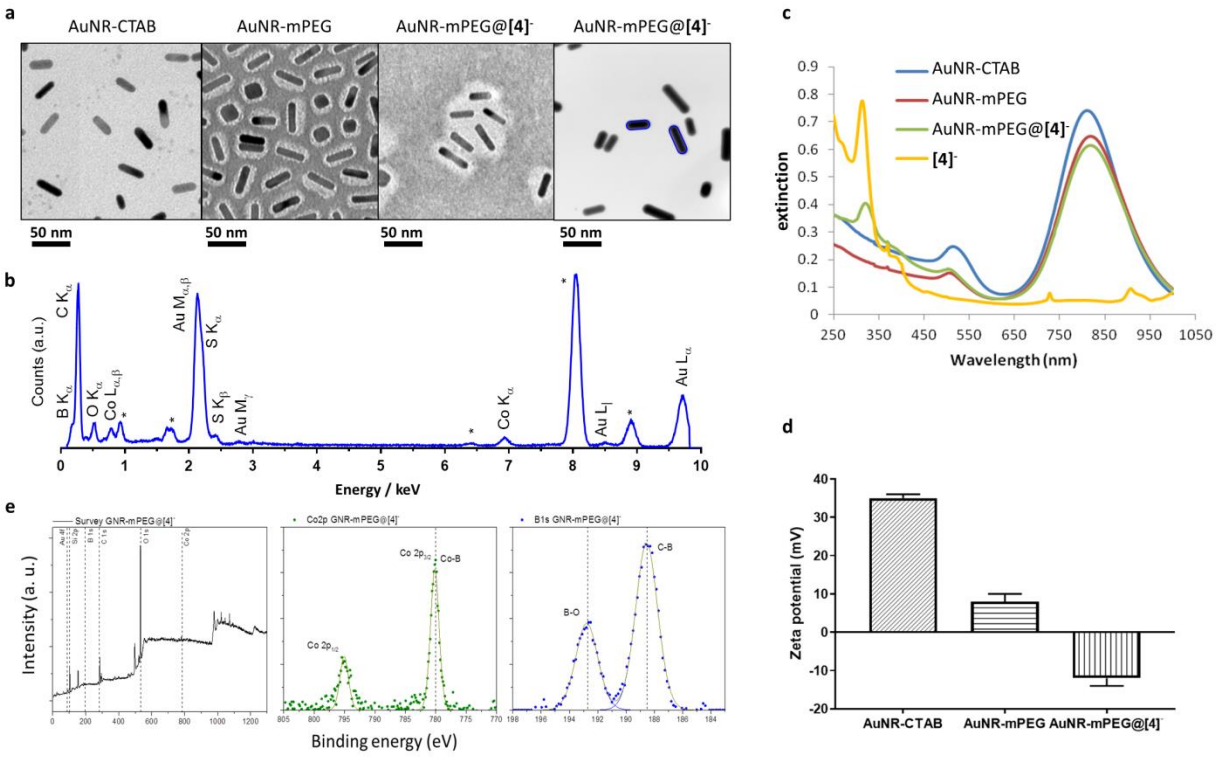

Figure 2: a) Representative transmission electron micrographs (TEM) of AuNR-CTAB, AuNR-mPEG and AuNR-mPEG@**[4]**$^-$, the latter two with negative staining; on the right, representative BF-STEM image of AuNR-mPEG@**[4]**$^-$ without staining. The areas analysed with EDXS are delineated in blue; b) sum EDXS spectrum of the selected AuNRs; c) UV-Vis-NIR extinction spectra of AuNR-CTAB, AuNR-mPEG, AuNR-mPEG@**[4]**$^-$ and compound **[4]**$^-$; d) ζ-potential values measured for AuNR-CTAB, AuNR-mPEG and AuNR-mPEG@**[4]**$^-$; e) XPS analysis of PEG-stabilized AuNRs@**[4]**$^-$.

Finally, COSAN derivatives were conjugated onto the AuNRs surface by incubating AuNR-mPEG with compound **[4]**$^-$ in ethanol for 2 h. After purification by centrifugation and repeated washing, boron-rich AuNRs (AuNR-mPEG@**[4]**$^-$) were obtained. The amount of

[4]$^-$ in the final AuNR-mPEG@**[4]**$^-$ was determined by ICP-MS from the difference between the amount of **[4]**$^-$ in the starting solution and in the supernatant/washings, as 225 μg per mg of gold, which results in *ca.* 100 μg of boron/mg of gold. The size and aspect ratio remained the same as for AuNR-mPEG (Figure 2a, SI Figure S1). While UV-Vis-NIR spectroscopy showed unchanged absorption maximum at 819 nm (Figure 2c), a new absorption band appeared at 320 nm, related to COSAN (yellow line in Figure 2c), which shows a maximum absorption at 314 nm, thus confirming successful adsorption of boron clusters on the AuNR surface. The recorded shift of the ζ-potential value, from +8±2 mV to -12±2 mV (Figure 2d), is in agreement with the attachment of negatively charged cobalt-*bis*(dicarbollide) complexes on the AuNR surface.

As additional structural evidence, the presence of COSAN on the surface was confirmed by scanning transmission electron microscopy (STEM) combined with energy-dispersive X-ray spectroscopy (EDXS). Energy bands in STEM-EDXS corresponding to cobalt and boron were observed, confirming the presence of **[4]**$^-$ on the surface of particles (Figures 2a and 2b). Furthermore, X-ray photoelectron spectroscopy (XPS) analysis of AuNRs-mPEG@**[4]**$^-$ showed a peak at 780.2 eV in the spectrum, corresponding to Co-B bonds, and peaks at 192.8 and 188.5 eV, corresponding to B-O and C-B bonds, respectively (Figure 2e).[36] These results further confirm the presence of both cobalt and boron on the AuNR surface.

It is well known that gold has a high cross-section for thermal neutrons.[37] Hence, the presence of gold at the core of the nanoconjugates might be perceived as a drawback for BNCT applications, as gold could eventually capture a fraction of the incident neutrons through the ^{197}Au(n,γ)^{198}Au nuclear reaction. Our calculations (see ESI for details) confirm that, considering the gold/boron composition of the nanoconjugates, and assuming a natural abundance of ^{10}B (20%), for every 15 reactions on ^{10}B there is only one reaction on ^{197}Au. In the case of a 100% abundance of ^{10}B (as used in BNCT) there is one reaction on ^{197}Au every

about 77 reactions on ^{10}B. Therefore, we conclude that the use of gold as a boron carrier is not a limitation for BNCT applications, at least considering the chemical composition of the nanoconjugates reported here.

Radiolabeling of AuNRs-mPEG@[4]$^-$ with ^{64}Cu

To enable subsequent biodistribution experiments using positron emission tomography (PET) imaging, we tackled the radiolabeling of AuNRs with a positron emitter. Previous studies carried out in our research group demonstrated the suitability of ^{124}I to radiolabel gold nanoparticles for subsequent investigation using PET.[25] However, this radionuclide is not widely available and in-house production was not established. Hence, we decided to explore an alternative strategy using ^{64}Cu and following a previously published method with minor modifications.[38-39] In brief, [^{64}Cu]$CuCl_2$ was reduced in the presence of hydrazine (N_2H_4) on the surface of AuNRs-mPEG@**[4]**$^-$ at room temperature for 1 h. After purification by centrifugation, radiochemical yields close to 70% were achieved. One fraction of [^{64}Cu]AuNRs-mPEG@**[4]**$^-$ was allowed to completely decay, and characterized by TEM, ζ-potential and UV-Vis-NIR spectroscopy (Figure S2). Both the size and aspect ratio of the nanorods were found to remain unaltered, and the UV-Vis-NIR spectrum showed two maxima at 819 nm and 320 nm, thereby confirming that the labeling process did not affect the main plasmonic properties of the AuNRs and that COSAN was still present. The recorded ζ-potential value was -13±2 mV.

The stability of the radiolabel is paramount when performing *in vivo* experiments because its detachment may lead to wrong interpretations of imaging data. The determination of the stability of the radiolabel *in vivo* is extremely challenging; hence, *in vitro* models are usually employed to mimic *in vivo* conditions.[40] When radiometals are employed for radiolabeling, one of the most conclusive approaches consists of incubating the labeled species in the presence of a chelator capable of sequestrating the radionuclide. We investigated the

radiochemical stability of [^{64}Cu]AuNRs-mPEG@**[4]**$^{-}$ by incubation in three different media at 37 °C. Irrespective of the medium and even in the presence of chelators, >92% of the initial ^{64}Cu remained attached to AuNRs-mPEG@**[4]**$^{-}$ at 48 h of incubation (Figure S3), thereby proving that the labeled AuNRs are sufficiently stable to tackle *in vivo* experiments.

***In vitro* studies: Cytotoxicity**

The nanoconjugates developed in the current work do not have a targeting moiety. Hence, accumulation in the tumor is expected to occur *via* the EPR effect. In this scenario, proof of concept experiments to evaluate *in vivo* tumor accumulation (see below) could be performed in any cancer model. In this work, we selected a xenograft mouse model of gastric adenocarcinoma, generated by subcutaneous inoculation of MKN-45 cells in immunodeficient mice, for two reasons: first, this is a well-established model in our laboratory;[41] second, gastric adenocarcinoma is the fourth most common malignancy worldwide and remains the second cause of death of all malignancies worldwide.[42] Hence, therapeutic alternatives to current clinical practice are urgently required. Before moving to *in vivo* studies, the cytotoxicity of AuNR-mPEG@**[4]**$^{-}$ was evaluated in this cancer cell line, together with HDFa cells as controls. With this aim, cells were incubated with 10, 20, 40, 60, 80, and 100 μM (gold concentration) of AuNRs for up to 72 h, prior to analysis using the MTT assay.

AuNR-mPEG@**[4]**$^{-}$ did not induce cell death at up to 100 μM (gold concentration) in any of the tested cell lines (Figure 3), indicating negligible cytotoxicity. Noteworthy, HDFa cells seem to show (non-significant) enhanced proliferation over time in the presence of the AuNR-PEG@**[4]**$^{-}$. Indeed, previous results reported in the literature showed that certain sizes and concentrations of gold nanoparticles have a promoting effect on cell proliferation,[43] and a similar effect to that observed here was reported for AuNRs including different

functionalizations.[44] As the observed trends lack statistical significance, investigation of the reasons behind this phenomenon was considered beyond the scope of the current work.

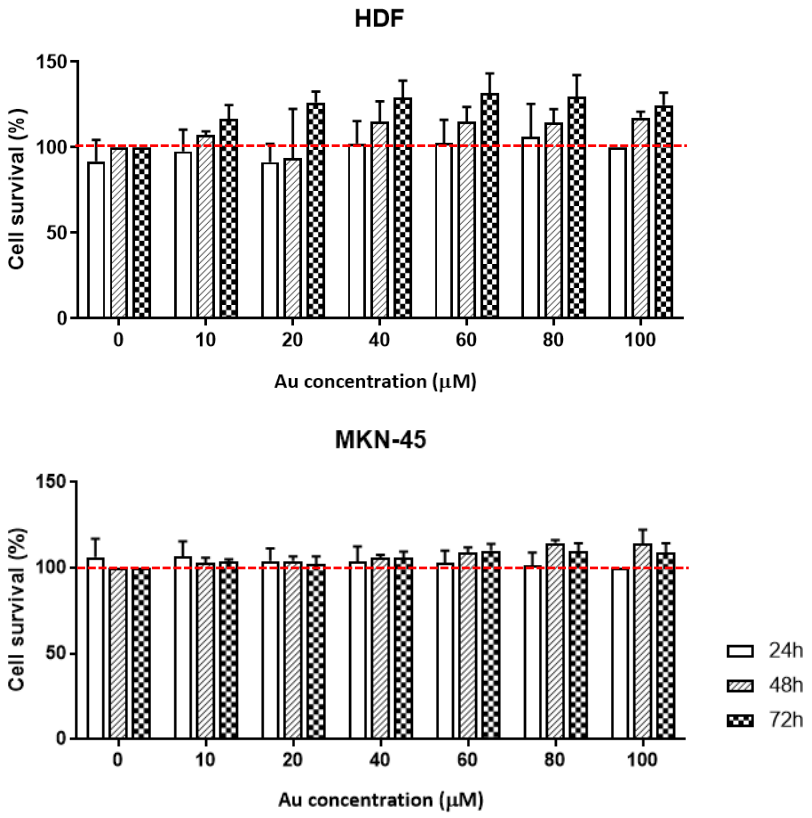

Figure 3. Cell viability in the presence of AuNR-mPEG@**[4]**$^-$ for 24, 48 and 72 hours: a) MKN-45 gastric cell line and b) human dermal fibroblasts (HDFa); in both cases, cells were incubated with increasing concentrations of AuNRs and cell viability was determined by the MTT assay. Data are shown as the mean ± standard deviation (error bars) of three independent experiments.

In vivo studies

In vivo imaging studies using PET in combination with Computerized Tomography (CT) were carried out in a human gastrointestinal adenocarcinoma mouse model (MKN-45 human cell line) after intravenous administration of [^{64}Cu]AuNR-mPEG@**[4]**$^-$. General biodistribution of the labeled AuNRs and accumulation in the tumor were determined by

acquiring static PET images at different time points after administration of the labeled particles (1, 4, 24 and 48 h; see Figures 4a-4d for representative images).

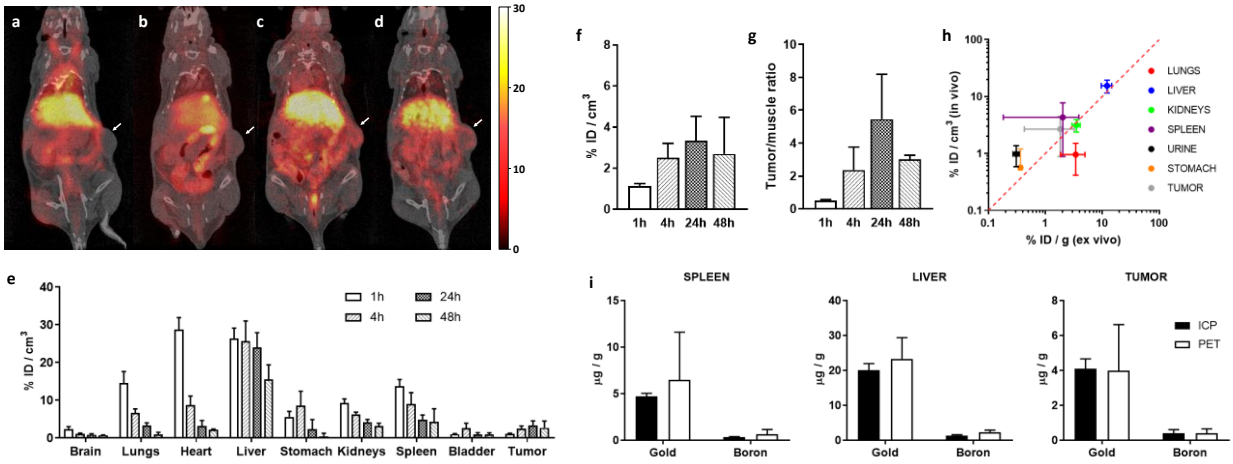

Figure 4. Representative PET images (coronal views) obtained at 1 (a), 4 (b), 24 (c), and 48 (d) hours after administration of [^{64}Cu]AuNR-mPEG@[4]- in a mouse bearing MKN-45 tumor. Maximum intensity projection (MIP) PET images were co-registered with representative CT coronal slices. The position of the tumor is indicated with white arrows; (e,f) accumulation of [^{64}Cu]AuNR-mPEG@**[4]**$^{-}$ in different organs (e) and the tumor (f) at different time points after intravenous administration, as determined by PET imaging; (g) tumor-to-muscle ratios at different time points; (h) correlation of results obtained by *in vivo* imaging and dissection/gamma counting. In all cases, values are expressed as mean ± standard deviation (n=4); (i) Amount of gold and boron in spleen, liver and the tumor at 48 hours after intravenous administration of [^{64}Cu]AuNR-mPEG@**[4]**$^{-}$, as determined by ICP-MS and PET imaging. Values for PET imaging are obtained by multiplying the %ID/cm^3 (values from Fig. 4f) by the relative load of boron and gold in the nanoconjugates.

Volumes of interest (VOIs) were drawn in major organs and tumor tissue based on reconstructed CT images, and used to quantify PET images. The concentration of radioactivity in each region was determined as percentage of injected dose per cubic

centimeter of tissue (%ID/cm^3) (Figure 4e). At t = 1 h, high accumulation of radioactivity was observed in the heart (28.7±3.2 %ID/cm^3), suggesting the presence of a significant amount of labeled AuNRs in the blood pool. This value progressively decayed with time, to reach a value of 2.22±0.16 %ID/cm^3 at t = 48 h. At t = 1 h, high accumulation of AuNRs was observed in the liver (26.3±2.8 %ID/cm^3), lungs (14.6±3.0 %ID/cm^3), and spleen (13.7±1.8 %ID/cm^3). In these organs, a progressive decrease of radioactivity concentration was observed over time, reaching values of 15.5±3.9 %ID/cm^3, 0.96±0.5 %ID/cm^3 and 4.3±3.4 %ID/cm^3, respectively, at t = 48 h after administration. These results suggest a moderate sequestration of NPs by organs of the mononuclear phagocyte system (MPS). Lower accumulation in kidneys (i.e. 9.3±1.0 %ID/cm^3), and no significant elimination via urine were also observed, suggesting a very slow glomerular filtration rate. A progressive decrease of the amount of AuNRs found in the liver and kidneys is important because this trend may reduce local side- or toxic effects in eventual long-term treatments.

The concentration of radioactivity in the tumor progressively increased with time (Figure 4f) to reach a maximum value at t = 24 h (3.3±1.2 %ID/cm^3) and slowly decreased thereafter (2.7±1.8 %ID/cm^3 at t = 48 h). The tumor-to-muscle ratio showed a similar trend, reaching a maximum of 5.4±2.7 at t = 24 h after administration (Figure 4g).

The results above are based on the assumption that AuNRs are chemically and radiochemically stable over the whole duration of the study, this is, that the imaging results reflect the real accumulation of AuNR-mPEG@**[4]**$^-$ in different organs and tumor tissue. In order to prove these assumptions and to unambiguously determine the amount of AuNR-mPEG@**[4]**$^-$ that reach different organs (liver and spleen) and the tumor, the concentration of boron and gold in selected organs were determined by ICP-MS (Figure 4i). A good correlation was achieved between results obtained by ICP-MS and by *in vivo* imaging, confirming the stability of our functionalized AuNRs and their capacity to reach the tumor.

In vivo biodistribution results were confirmed by *ex vivo* gamma-counting experiments, conducted immediately after finalizing the last imaging session. Mice were sacrificed, organs of interest were harvested and the amount of radioactivity in each organ was measured in an automated gamma-counter (Wallach Wizard, PerkinElmer, Waltham, MA, USA). As depicted in Figure 4h, there is a good correlation between *in vivo* and *ex vivo* results.

Our biodistribution data are in good agreement with literature results for other AuNRs. In one such example, non-targeted, PEG-stabilized AuNRs were evaluated in a xenograft mouse model of breast cancer and maximum accumulation in the tumor was observed at 6–24 hours after administration, with values slightly above 5% ID/g. These uptake values could be significantly increased by covalently attaching a bombesin peptide to the AuNRs. The authors also observed high accumulation in the liver and kidneys.[45] In a more recent work,[46] larger (93.4 nm in length, 24.8 nm in width; aspect ratio = 3.8) PEG-stabilized AuNRs functionalized with Arg-Gly-Asp- (RGD-) peptides were assayed in a mouse model of melanoma generated by subcutaneous inoculation of $\alpha_v\beta_3$-positive B16F10 mouse malignant melanoma cells. Maximum accumulation at 6 h after administration was observed in liver (26.51±4.93 %ID/g), lungs (7.07±0.25 %ID/g), and spleen (5.55±0.69 %ID/g), while accumulation in the tumor was 5.09±0.68 %ID/g and the tumor-to-muscle ratio was *ca.* 10.

In order to predict BNCT therapeutic efficacy, we calculated the amount of boron accumulated in the tumor at different times after administration, based on PET imaging results. Considering that: (i) the injected dose to the animal was 150 μg of AuNR-mPEG@**[4]**$^-$ (amount of gold); (ii) AuNRs contain 100μg boron per mg of gold; and (iii) the concentration of AuNRs in the tumor at t = 24 h after administration was 3.3±1.2 %ID/cm^3, the average concentration of boron in the tumor at t = 24 h was 0.5 μg/cm^3, and the maximum concentration of gold in the tumor was ca. 5 μg/cm^3. As demonstrated in our *in vitro* therapeutic experiments (see below), these values may suffice to guarantee therapeutic

efficacy *in vivo* under NIR or neutron irradiation. Moreover, higher tumor accumulation could be easily achieved by administering higher or repeated doses.

PTT efficacy studies *in vitro*

Further insight into the potential therapeutic capacity of our nanoconjugates was gathered by investigating the efficiency of AuNRs toward localized thermal heating under NIR irradiation *in vitro*. For that purpose, cellular spheroids were chosen as the study model since their physiological behavior more closely resembles that of cells in tumors, as compared to 2D monolayer cultures.[47] Prior to incubating spheroids with AuNRs, we determined the photothermal efficiency (43%) of AuNR-mPEG, with and without the COSAN ligand. A solution of AuNRs (Au concentration = 20 μg/mL; B concentration = 2 μg/mL) was exposed to NIR laser irradiation resonant with the AuNR LSPR peak at ~ 800 nm. We observed nearly identical heating profiles for both AuNRs, and the decay fitting equation shows extremely similar photothermal efficiency profiles. Post-irradiation TEM analysis confirmed negligible laser-induced AuNR reshaping, supporting the use of these AuNR concentration and laser power density for cellular hyperthermia studies (See ESI, Figure S4).

Spheroids generated from MKN-45 and HDFa cells were incubated with AuNRs (concentration = 20 μg/mL in gold; 2 μg/mL in boron) and then submitted to 808 nm NIR laser irradiation, both before (group A) and after (group B) removing the media containing AuNRs. Control groups included: Group C, spheroids incubated in the absence of AuNRs and not submitted to laser irradiation; group D, spheroids incubated in the absence of AuNRs and submitted to laser irradiation; and Group E, spheroids incubated in the presence of AuNRs and not submitted to laser irradiation.

Highest spheroid cell viability was observed for group E (Figure 5a), consistent with the previous finding that the presence of gold nanorods enhances cell proliferation (see Figure 3),

although this increase was not statistically significant when compared to group D ($p = 0.073$). Noteworthy, no increase in temperature was detected when the spheroids were not irradiated (groups C and E; Figure 5b) or when spheroids were irradiated in the absence of AuNRs (group D). When spheroids incubated with AuNRs for 48 h were irradiated, an average temperature increase of *ca.* 1 °C was detected (Group B; Figure 5b and Figure S5), and cell viability decreased by *ca.* 20% with respect to group E ($p < 0.0001$). The irradiation of cells with AuNRs present in the media resulted in a temperature increase during heating of *ca.* 23 °C (Figure 5b and Figure S5), and a decrease in cell viability of *ca.* two orders of magnitude with respect to groups B-E ($p < 0.0001$ in all cases). The lower heating and subsequent cell death observed in Group B with respect to Group A suggests that cell internalization of AuNRs in the 3D cell model is slow. However, the large increase in local temperature when irradiation was conducted in the presence of AuNRs (Group A) confirms the suitability of the nanoconjugates to induce cell damage at concentrations within the range of those achieved in the tumor in our preclinical experiments.

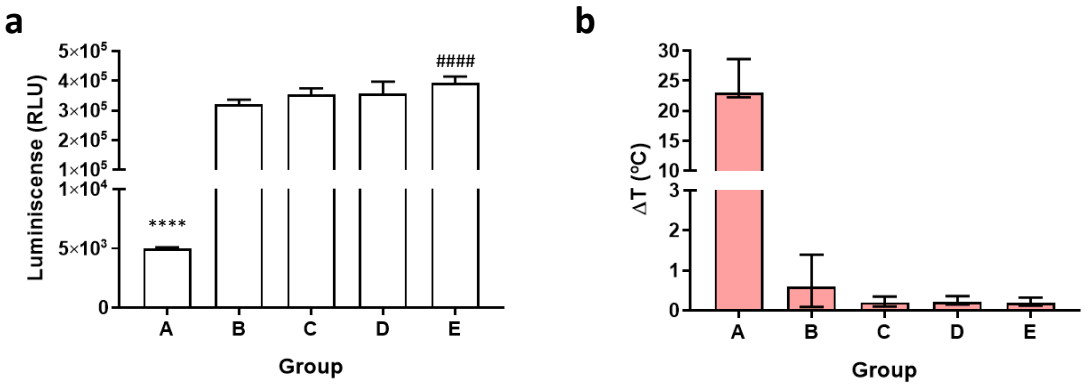

Figure 5. a) Cell survival of spheroids in different experimental scenarios, as measured using the CellTiter-Glo® 3D Cell Viability Kit. Group A: spheroids incubated with AuNRs (concentration = 20 µg/mL in gold) followed by NIR irradiation; B: spheroids incubated with AuNRs followed by media exchange and NIR irradiation; Group C: spheroids incubated in the absence of AuNRs, no laser irradiation; Group D, spheroids incubated in the absence of

AuNRs and submitted to laser irradiation; and Group E, spheroids incubated in the presence of AuNRs, no irradiation. On average 6 spheroids were assayed per group (N = 6) and values are expressed as mean ± standard deviation (n=4); probability values for differences with respect to Groups B-D are depicted as **** $p < 0.0001$; probability values for differences with respect to group B are depicted as $^{\#\#\#\#}p < 0.0001$; b) temperature increase of the irradiated wells for groups A-E. Values represent the increase in temperature reached after 10 min irradiation with respect to room temperature; upper whisker: standard deviation of the temperature measured in the irradiated sample; lower whisker: standard deviation of measured room temperature.

Internalization in spheroids

In order to shed light on the reasons behind the unexpectedly low photothermal effect observed for group B (spheroids incubated with AuNRs followed by media exchange and NIR irradiation), we decided to further investigate the uptake of AuNR-mPEG@**[4]**$^-$ in spheroids, using a combination of microscopy and analytical techniques. With that aim, spheroids composed of MKN45 and HDFa cells were produced, incubated in the presence of AuNR-mPEG@**[4]**$^-$ (0.1 mM Au concentration; 100 µL) for 24h, and further processed to their subsequent analysis (see experimental section for details). Inductively coupled plasma mass spectrometry (ICP-MS) analysis revealed an average uptake of 12.6 ± 4.2 ng Au/spheroid (64 pmol Au/spheroid), which corresponds to 0.64% of the amount of AuNR-mPEG@**[4]**$^-$ in the incubation media. These results explain the modest temperature increase achieved during laser irradiation of group B spheroids (*ca.* 1 °C, see Figure 5b). Laser irradiation of an aqueous solution of AuNR-mPEG@**[4]**$^-$ at a concentration of 64 pmol/100 µL, resulted in a temperature increase of ca. 0.8 °C (see ESI, Figure S6), thus supporting the ICP-MS results.

Both reflection and multiphoton confocal microscopies showed modest internalization, with AuNRs located mainly at the outer edge of the spheroids (Figure 6b). No signal could be observed in the control sample using multiphoton confocal microscopy, as expected in the absence of AuNRs. Differences between AuNR-incubated and control samples using reflection confocal microscopy could be observed only when images were represented as z-stack maximum intensity projections, clearly revealing AuNR internalization from the outer edge of the spheroid (Figures 6c and 6d). Finally, to verify that the low heating observed in spheroids after NIR irradiation was not due to an LSPR shift occurring intracellularly, we obtained TEM images of cells extracted from an external layer of the spheroids, to gather the level of aggregation of AuNRs after cell internalization (Figure 6e). The images clearly showed the presence of non-aggregated AuNRs inside cellular vesicles, supported by the data shown in SI (Figure S4) confirming the lack of laser-induced AuNR reshaping.

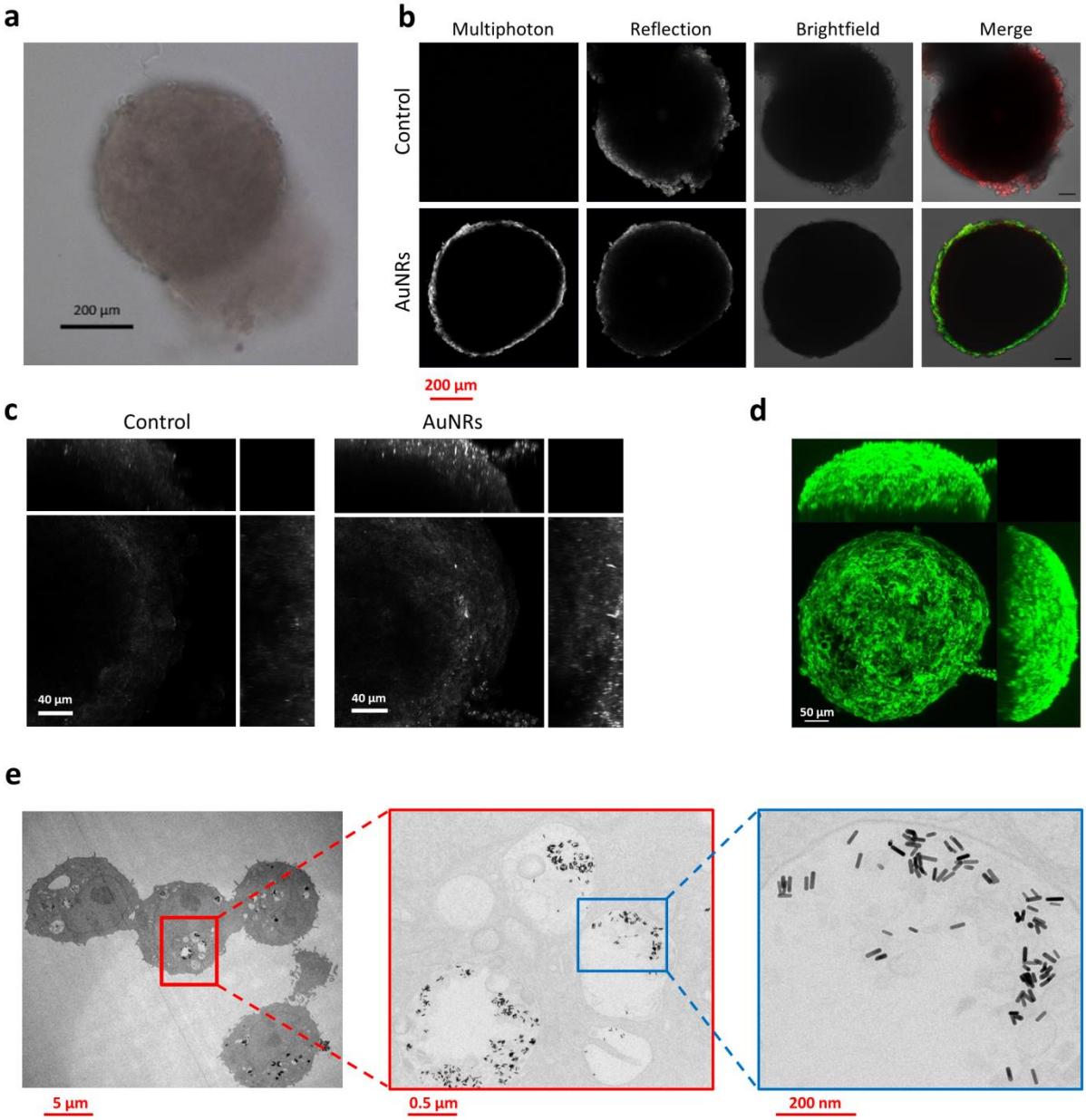

Figure 6. a) Bright field image of an MKN:HDFa spheroid. b) Optical microscopy images of MKN:HDFa spheroids incubated with (AuNRs) and without (control) AuNR-mPEG@**[4]**$^{-}$. Photos were taken at a distance of 100 µm from the glass coverslip. Multiphoton (green in merged images) and reflection (red in merged images) images are maximum intensity projections (MIP) of a thickness of 20 µm from a total of 90 – 110 µm. A 3-pixel filter was applied prior to forming the MIP image. The final merge image was obtained using ImageJ. c) Optical microscopy images of MKN:HDFa spheroids incubated with (AuNRs) and without (control) AuNR-mPEG@**[4]**$^{-}$, obtained with reflectance imaging, covering the section of

spheroid closest to the objective and measuring 80 μm in thickness. Orthodoxal images show the entire 80 μm compressed as a MIP image. d) Orthodoxal views (MIPs) of z-stacks of spheroids incubated with AuNR-mPEG@**[4]**$^-$, obtained with multiphoton microscopy (ex 780nm, ex 575-610nm). 282 slices were captured, equivalent to 171 μm in thickness, starting closest to the objective. e) TEM images of cells extracted from an external layer of the spheroids, showing AuNR-mPEG@**[4]**$^-$ uptake. Magnification is increased from left to right.

BNCT studies *in vitro*

We finally investigated the potential of our AuNRs as BNCT agents in cells. Therapeutic experiments in cells can be performed by incubating the cells with the boron-rich agent to achieve internalization, and then submitting the cells to neutron irradiation after media exchange. In our case, however, and in view of the low internalization capacity of the NPs suggested by PTT studies in spheroids, we exposed the cells to AuNR-mPEG@**[4]**$^-$ at different concentrations, and submitted the mixture to neutron irradiation without exchanging the media. This approach mimics *in vivo* scenarios in which the boron-rich agent stays at the extracellular matrix of the tumor environment. Experimentally, MKN-45 cells were incubated with AuNRs (concentrations = 0.1 and 10 μg/mL in boron, equivalent to 5 and 500 μM in gold, respectively; groups I and II) and the mixtures were irradiated with thermal neutrons. Control groups included: Group III, cells incubated in the absence of AuNRs and not submitted to neutron irradiation; group IV, cells incubated in the presence of AuNRs (0.1 μg/mL in boron) and not submitted to neutron irradiation; group V, cells incubated in the presence of AuNRs (10 μg/mL in boron) and not submitted to neutron irradiation; and group VI, cells incubated in the absence of AuNRs and submitted to neutron irradiation.

High cell survival was observed for groups III-V (74.1-85.6% cell viability, see Table 1), confirming that in the absence of neutron irradiation, AuNRs do not show toxicity toward this cell line. Cell viability decreased to 58.4% ($p < 0.0001$ with respect to groups III-V) when

cells not exposed to AuNRs were irradiated with neutrons (group VI), suggesting that under the irradiation conditions assayed, neutrons alone significantly decrease cell survival. When cells incubated with AuNRs at a concentration of 0.1 μg/mL in boron were irradiated, cell viability further decreased to 52.3% ($p < 0.0001$ with respect to group VI), and this value further decreased to 22.1% when cells were incubated with AuNRs at a concentration of 10 μg/mL in boron. Altogether, these results confirm the suitability of AuNR-mPEG@**[4]**$^-$ nanoconjugates to induce cell damage under neutron irradiation, at concentrations below those achieved in the tumor in our *in vivo* experiments (0.5 μg/mL in boron).

Table 1. Cell survival fraction after incubation of MKN-45 cells with AuNR-mPEG@**[4]**$^-$ at different concentrations and subsequent neutron irradiation (and corresponding controls).

Cell group (treatment conditions)	Survival fraction (mean ± standard deviation)
I (neutron irradiation, AuNRs at 0.1 μg/mL in boron)	52.3 ± 0.25%
II (neutron irradiation, AuNRs at 10 μg/mL in boron)	22.1 ± 0.6%
III (no neutron irradiation, no AuNRs)	85.6 ± 0.4%
IV (no neutron irradiation, AuNRs at 0.1 μg/mL in boron)	82.8 ± 0.8%
V (no neutron irradiation, AuNRs at 10 μg/mL in boron)	74.1 ± 1.6%
VI (neutron irradiation, no AuNRs)	58.4 ± 0.3 %

In conclusion, we have demonstrated that PEG-stabilized, COSAN functionalized AuNRs can be efficiently prepared and radiolabeled with ^{64}Cu. Labeled nanoconjugates have favorable *in vivo* pharmacokinetics and show significant accumulation in the tumor and good tumor-to-muscle ratios at 24–48 hours after administration. Such multidecorated AuNRs carry large amounts of boron, hence bearing the potential to become a valuable tool for the development of nanoparticle-based BNCT agents, as demonstrated in our *in vitro* assays. This, together with the capability to absorb NIR light and induce localized temperature increase and thermal damage opens new avenues for their use in combined therapies.

Limitations of the study

To the best of our knowledge, our work reports the first example of gold nanocomposites suitable for combined PTT and BNCT therapies. Still, our AuNRs present certain limitations.

First, the amount of nanorods accumulated in the tumor under current experimental conditions is low to provide BNCT therapeutic efficacy, as the boron concentration values achieved in the tumor are 10-30 times below the widely accepted threshold of 15-20 μg of boron per gram of tumor. Still, therapeutic effect was observed at concentrations as low as 0.1 μg/mL *in vitro*. The concentration of gold is in the range of that showing therapeutic efficacy *in vitro*. Tuning the size, aspect ratio, and surface functionalization of the nanoconjugates may enhance circulation time, minimize sequestration by the organs of the MPS and hence improve tumor accumulation. Also, other administration alternatives such as intra-tumor administration may enhance the accumulation of boron atoms in the target tissue. These options are currently being explored in our laboratory.

Another major limitation is the possibility to conduct combined therapeutic studies with two therapeutic approaches that are technically challenging, especially in the case of BNCT. The installation of accelerator-based neutron sources and the possibility to implement optical fiber-based laser systems should mitigate this limitation.

EXPERIMENTAL

Materials

Caesium cobalt(III) *bis*(dicarbollide) (COSAN) (Katchem Ltd., Prague, Czech Republic), hexadecyltrimethylammonium bromide (CTAB, Sigma-Aldrich), gold(III) chloride trihydrate ($HAuCl_4 \cdot 3H_2O$, Aldrich), sodium borohydride ($NaBH_4$, Aldrich), silver nitrate ($AgNO_3$, Sigma-Aldrich), ascorbic acid (Sigma-Aldrich), potassium carbonate (K_2CO_3, Sigma-Aldrich), poly (ethylene glycol) methyl ether thiol (mPEG-SH, MW 5000, Sigma-Aldrich), and hydrazine hydrate (50–60%) (Sigma-Aldrich) were used as purchased. All other reagents and anhydrous solvents, stored over 4 Å molecular sieves, were purchased from Sigma-Aldrich Chemical Co. (Madrid, Spain) and used without further purification. HPLC grade

ethanol, methanol, and acetonitrile were purchased from Scharlab (Sentmenat, Barcelona, Spain).

Experiments were carried out, except where otherwise noted, under dry, oxygen-free dinitrogen atmosphere. Analytical thin layer chromatography (TLC) measurements were conducted with silica gel 60 F_{254} plates (Macherey-Nagel). Milli-Q water (resistivity 18.2 MΩ·cm at 25 °C) was used in all experiments. All glassware was washed with aqua regia.

Instrumentation

^{1}H-NMR (500 MHz), ^{13}C-NMR (126 MHz) and ^{11}B-NMR (160 MHz) spectra were recorded on a 500-MHz Avance III Bruker spectrometer. All NMR spectra were performed in deuterated solvents at 22 °C. ^{11}B-NMR shifts were referenced to external $BF_3 \cdot OEt_2$, whereas ^{1}H and ^{13}C-NMR shifts were referenced to $SiMe_4$. Chemical shifts are reported in units of parts per million (ppm) downfield from the reference peak and all coupling constants are reported in Hertz (Hz).

UPLC/ESI-MS analyses were performed using an AQUITY UPLC separation module coupled to LCT TOF Premier XE mass spectrometer (Waters, Manchester, UK). An Acquity BEH C18 column (1.7 µm, 5 mm, 2.1 mm) was used as stationary phase. The elution buffers were A (water and 0.1% formic acid) and B (methanol and 0.1% formic acid). The column was eluted with the following gradient: t=0 min, 95% A, 5% B; t=0.5 min, 95% A, 5% B; t=5.5 min, 25% A, 75% B; t=16 min, 1% A, 99% B; t=20min, 1% A, 99% B. Total run was 20 min, injection volume was 5 µL and flow rate 300 µL/min. The detection was carried out in both negative and positive ion modes, monitoring the most abundant isotope peaks from mass spectra ($M\text{-}H^+$) or ($M+H^+$).

Transmission electron microscopy (TEM) was performed using a JEOL JEM-1400 plus microscope (JEOL, Tokyo, Japan) working at an acceleration voltage of 120 kV. The carbon film of copper grids (CF400-Cu, Electron Microscopy Sciences) was treated under air plasma

in a glow discharge system (Emitech K100X, 40mA during 2 min) just before sample preparation. For TEM examinations, a single drop (1 μL) of the nanoparticles (NPs) solution was placed onto a copper grid coated with a carbon film After 1 min, the drop was removed with filter paper and the sample was incubated with 3 μL of uranyl acetate 0.5% (3 min). The drop was removed with filter paper and the grid placed on top of a drop of water twice and dried with a filter paper. Scanning transmission electron microscopy (STEM) images were taken in a JEOL JEM-2100F (200kV, HAADF detector, coupled with an EDXS-INCA Oxford system). Energy dispersive X-ray spectroscopy (EDXS) of selected areas was carried out for 30 min, in which the sample displacement was automatically corrected every 2 min. A clear grid region without particles was analyzed to evaluate the presence of scattered signals coming from the detector, grid and equipment microscope composition (copper, silicon and iron, among others). These non-relevant signals were omitted (<0.1 keV) or asterisk-labeled in the spectrum.

XPS experiments were performed in a SPECS Sage HR 100 spectrometer with a non-monochromatic X-ray source (aluminium Kα line of 1486.6 eV energy and 252 W), placed perpendicular to the analyzer axis and calibrated using the 3d5/2 line of Ag with a full width at half maximum (FWHM) of 1.1 eV. The selected resolution for the spectra was 15 eV of Pass Energy and 0.15 eV/step. All measurements were made in an ultra-high vacuum (UHV) chamber at a pressure around 6×10^{-8} mbar. An electron flood gun was used for charge neutralisation. Gaussian Lorentzian functions were used for fittings (after a Shirley background correction) where the FWHM of all the peaks were constrained, while the peak positions and areas were set free. The main C1s peak was used for charge reference and set at 284.8 eV.

Inductively coupled plasma mass spectrometry (ICP-MS) measurements were performed on a Thermo iCAP Q ICP-MS (Thermo Fisher Scientific GmbH, Bremen, Germany). An

ASX-560 auto-sampler was coupled to the ICP-MS (CETAC Tech, Omaha, NE, USA). UV-Vis-NIR spectra were measured in an Agilent 8453 UV-Vis-NIR diode-array spectrophotometer. Dynamic light scattering (DLS) and ζ-potential measurements were performed in water at neutral pH using a Malvern Zetasizer Nano ZS system (Malvern Instruments, Malvern, UK).

Chemistry

Synthesis of [3,3'-Co(8-$C_5H_{10}O$-1,2-$C_2B_9H_{10}$)(1',2'-$C_2B_9H_{11}$)] (2): The synthesis of compound **2** was carried out following a previously reported method.[31] In brief, to a mixture of tetrahydropyran (THP, 14 mL), $[Co(C_2B_9H_{11})_2]^-$ (cesium salt, 2.0 g, 4.38 mmol), and dimethyl sulfate (0.86 mL, 8.76 mmol), sulfuric acid (0.24 mL, 3.94 mmol) was added drop-wise and the mixture was heated at 80 °C for 10 h with continuous stirring. The reaction mixture was filtered and the filtrate was evaporated under vacuum at room temperature. Purification by column chromatography using dichloromethane yielded compound **2** as an orange solid (1.2 g, 68%).

^{1}H NMR (500 MHz, $CDCl_3$, δ): 4.66 [2H, s, C_c–H], 4.36 [2H, s, C_c–H], 3.98 [4H, CH_2–O], 1.77 [4H, m, CH_2], 1.50 [2H, m, CH_2]; ^{11}B NMR (160 MHz, $CDCl_3$, δ): 24.27 [1B, s], 8.15 [1B, d], 4.31 [1B, d], -3.07 [1B, d], -4.35 [4B, d], -8.12 [2B, d], -9.47 [2B, d], -15.40 [2B, d], -18.86 [2B, d], -21.29 (1B, d), -26.82 [1B, d]; LCMS (ESI) Experimental $[M]^-$ m/z = 407.20 (theoretical $[M]^-$ m/z = 407.86).

Synthesis of [3,3']-Co(8-CH_3-CO-S-$(CH_2)_5$-O-1,2-$C_2B_9H_{10}$)(1',2'-$C_2B_9H_{11}$)]$^-$ ([3]$^-$): To a solution of **2** (750 mg, 1.209 mmol) in N,N-dimethylformamide (DMF; 8 mL), potassium thioacetate (165.7 mg, 1.451 mmol) was added and stirred at room temperature for 14 h. For the workup, 50 mL of water was added and extracted with ethyl acetate (3×50 mL); the organic layers were combined and washed with cold water and brine solution before drying over anhydrous sodium sulfate. The solvent was evaporated, and the crude was purified using

column chromatography (silica gel, 10% methanol in dichloromethane) to yield **[3]**$^-$ as yellow solid (705 mg, 84%).

^{1}H NMR (500 MHz, Methanol-d_4, δ): 4.15 [2H, s, C_c–*H*,], 4.07 [2H, s, C_c–*H*,], 3.49 [2H, t, C*H*$_2$O,], 2.87 [2H, t, C*H*$_2$-CH$_2$O,], 2.31 [3H, C*H*$_3$,], 1.56 [2H, p, C*H*$_2$-S], 1.50 [2H, q, C*H*$_2$-CH$_2$S], 1.43 – 1.36 [2H, m, C*H*$_2$-CH$_2$CH$_2$O]; ^{11}B NMR (160 MHz, Methanol-d_4, δ): 23.02[1B, s], 4.62 [1B, d, ^{1}J(B-H)=140.3], 0.47 [1B, d, ^{1}J(B-H)=143.3], -2.16 [1B, d, ^{1}J(B-H)=142.8], -4.59 [2B, d, ^{1}J(B-H)=138.7], -8.05 [6B, td, *J* 162.8, 150.9, 63.5], -17.29 [2B, d, ^{1}J(B-H)=154.4], -19.04 – -21.48 [2B, d], -21.40 – -24.13 [1B, d], -28.34 [1B, d, ^{1}J(B-H)=159.4]; ^{13}C NMR (126 MHz, Methanol-d_4,–δ): 68.93, 53.54, 46.70, 30.89, 29.21, 29.14, 28.61, 25.10; LCMS (ESI) Experimental [M]$^-$ m/z = 482.66 (theoretical [M]$^-$ m/z = 482.98).

Synthesis of [3,3']-Co(8-SH-(CH$_2$)$_5$-O-1,2-C$_2$B$_9$H$_{10}$)(1',2'-C$_2$B$_9$H$_{11}$)]$^-$ ([4]$^-$): To a solution of **[3]**$^-$ (890 mg, 1.440 mmol) in methanol (30 mL), sodium methoxide (77.8 mg, 1.440 mmol) was added and stirred at room temperature for 14 h. For the workup, reaction mixture was neutralized with IR-120 resin (3 g), filtered and washed with 10 mL of methanol. Combined methanol layers were concentrated and purified using column chromatography (silica gel, 12% methanol in dichloromethane) to yield **[4]**$^-$ as a yellow solid (505 mg, 61%).

^{1}H NMR (500 MHz, Methanol-d_4, δ): 4.16 [2H, bs, C_c–*H*], 4.08 [2H, bs, C_c–*H*], 3.51 [2H, t, C*H*$_2$O], 2.69 [2H, t, C*H*$_2$-CH$_2$O], 1.60 [2H, p, C*H*$_2$-S], 1.51 [2H, dq, C*H*$_2$-CH$_2$S], 1.42 [2H, qd, C*H*$_2$-CH$_2$CH$_2$O]; ^{11}B NMR (160 MHz, Methanol-d_4, δ): 23.02 [1B, s], 4.69 [1B, d, ^{1}J(B-H)=140.0], 0.43 [1B, d, ^{1}J(B-H)=142.0], -2.19 [1B, d, ^{1}J(B-H)=144.5], -4.64 [2B, d, ^{1}J(B-H)=142.4], -6.24 – -11.84 [6B, m], -17.33 [2B, d, ^{1}J(B-H)=157.7], -20.51 [2B, d, ^{1}J(B-H)=159.0], -22.59 [1B, d], -28.49 [1B, d, ^{1}J(B-H)=174.3]; ^{13}C NMR (126 MHz, Methanol-d_4): 69.08, 53.46, 46.70, 33.90, 30.83 , 24.71, 23.65; LCMS (ESI) Experimental [M]$^-$ m/z = 440.52 (theoretical [M]$^-$ m/z = 440.94).

Synthesis on multi-functionalized gold nanorods

Seedless synthesis of gold nanorods*:* Gold nanorods (AuNRs) were synthesized following a seedless growth method.[32] First, $HAuCl_4$ (100 µL, 0.05 M) was added to 10.0 mL of hexadecyltrimethylammonium bromide(CTAB; 0.1 M) at 27 ºC and shaken until the formation of the complex. Then, $AgNO_3$ (250 µL, 4.0 mM) was added, and the solution was gently shaken. HCl (12.0 µL, 37 wt. %) was added to obtain a pH close to 1.0, followed by addition of 70 µL of ascorbic acid (78.8 mM) under gentle stirring until the solution became clear. In the final step, ice-cold $NaBH_4$ (10 µL, 0.01 M) was injected into the growth solution and allowed to react for 6 h. The growth solution was maintained at 27 °C in a water bath. The synthesized AuNRs were centrifuged twice at 10,000×g to remove the excess CTAB as well as other reagents, and re-dispersed in water.

Synthesis of PEG-modified AuNRs (AuNR-mPEG): A AuNR solution was centrifuged at 10,000×g for 10 min, decanted, and resuspended in water to remove excess CTAB. A freshly prepared thiol-terminated PEG solution (300 µL, 10 mM, mPEG-SH) was added dropwise to the centrifuged AuNR solution (2 mL; 1 mM Au atoms). The mixed solution was stirred for 24 h at room temperature and centrifuged twice at 10,000×g for 10 min, decanted, and re-suspended in water to remove excess of PEG reagent.

Synthesis of PEG-stabilized, COSAN-functionalized AuNRs (AuNR-mPEG@[4]$^-$): To PEG-modified AuNRs (2 mL; [Au] = 1 mM) a fresh solution of COSAN-SH [**4**]$^-$ in ethanol (150 µL; 3 mg/mL) was quickly added and stirring was maintained for 2 h. The resulting NPs were centrifuged at 8,000×g for 20 min and resuspended in ultrapure water three times to remove excess COSAN-SH reagent, and re-dispersed in 1.0 mL of ultrapure water.

Synthesis of ^{64}Cu-labeled, functionalized gold nanorods ([^{64}Cu]AuNR-mPEG@[4]$^-$): $^{64}CuCl_2$ was produced by proton irradiation of ^{64}Ni as previously described,[48] and obtained as a solution in 0.1M HCl. A fraction of this solution containing ca. 20 MBq was evaporated to

dryness and the residue was dissolved in 0.4 M ammonium acetate buffer (pH 5.5). The resulting solution was added drop-wise into a solution containing AuNR-mPEG@**[4]**$^-$ ([Au]=250 μg/mL). After stirring for 5 min, hydrazine hydrate (3 μmol) was added and the solution was allowed to react at room temperature for 1 h and then washed by centrifugation to remove excess reagents, as well as unreacted ^{64}Cu. The labeling efficiency was calculated as the ratio between the amount of radioactivity present in the AuNRs after washing and the starting amount of radioactivity. One fraction of the [^{64}Cu]AuNRs-mPEG@**[4]**$^-$ sample was allowed to decay completely (ca. 8 half-lives) and subsequently analyzed by TEM and UV-Vis-NIR to confirm that the properties remained unaltered.

The radiochemical stability of [^{64}Cu]AuNRs-mPEG@**[4]**$^-$ was investigated by incubation in three different media at 37 °C: (i) Physiological saline solution containing EDTA as a chelator (0.9% NaCl + 2.5 mM EDTA); (ii) phosphate buffered saline containing EDTA (PBS + 2.5 mM EDTA); and (iii) mouse serum. At different time points, the nanorods were separated by centrifugation and the amounts of radioactivity in the pellet and in the supernatant were determined. The fraction of ^{64}Cu attached to the nanorods was calculated as the ratio between the amount of radioactivity in the pellet and the total amount of radioactivity (pellet + supernatant).

***In vitro* studies**

Cytotoxicity studies: To determine cell viability, MKN-45 human cancer cells and human dermal healthy fibroblasts (HDFa) were incubated with the AuNRs over 24, 48, and 72 h. Cells were seeded (3×10^4 cells/well, 100 μL/well, 96-well plate), allowed to adhere overnight in complete media (10% Fetal Bovine Serum (FBS) and 1% Penicillin/Streptomycin in RPMI 1640 medium for MKN-45 cells; DMEM medium for HDFa cells) and maintained in a humid atmosphere at 37 °C and 5% CO_2. Then, media was removed and cells were left untreated (blank) or incubated with the AuNR-containing

formulations, diluted accordingly in media. The experiments were performed in triplicates. After the desired time, cell supernatant was removed and 100 µL/well of MTT reagent (Roche), diluted in the corresponding media to the final concentration of 0.25 mg/mL, was added. After 1 h incubation at 37 °C and 5% CO_2, excess reagent was removed, and formazan crystals were solubilized by adding 200 µL of DMSO per well. The optical density of each well was measured in a TECAN Genios Pro 96/384 microplate reader at 550 nm. Data were plotted as the percentage of cell survival compared to control wells.

Photothermal therapy *in vitro* experiments: For the formation of MKN-45/HDFa spheroids, both cell lines were grown separately and then co-cultured in non-adherent U-shaped 96-well plates for 48-72 h in a 1:1 ratio (total cell number 8.6×10^4 cells/mL, 200 µL/well). Spheroids were grown, one per well, and those morphologically more homogeneous were separated in 5 groups (A-E). Those from groups A, B and E were incubated with AuNR-mPEG@**[4]**$^-$ (20 µg/mL) in FBS-free medium. Cells from groups C and D were incubated in medium (FBS-free medium; 1:1 DMEM-RPMI; total volume: 200 µL). At t = 48 h after incubation, spheroids were washed (except Group A) and transferred to flat-bottom 96-well sterile plates. Empty wells were left between samples for isolation reasons. Irradiation was performed with a Lumics GmbH IR diode laser (LU0808T040; collimated and focused at the exit of the fiber; spot size: 1.1 cm^2) with an excitation wavelength of 808 nm and irradiation power of 2.3 W/cm^2. The irradiation area of the well was *ca.* 0.8 cm^2. Irradiations were performed sequentially in each individual well for 10 min, with the plastic cover lid on to keep sterility. Temperature was recorded with a thermal camera FLIR A35, at a rate of 60 Hz. To measure the photothermal efficiency, 1 ml of AuNR solution was placed in a 1cm cuvette. The same power density and AuNR concentration was used as in spheroid experiments and the temperature was recorded with the same thermal camera as in *in vitro* experiments.

After irradiation, spheroids were transferred again to 3D culture plates and maintained there for 48 h before undertaking cell viability tests. These were carried out using CellTiter-Glo® 3D Cell Viability Assay (Promega), system following the manufacturer's guidelines. In brief, spheroids were washed with complete culture medium and transferred in 50 µL of medium to a white luminescence 96-well plate. Then, 50 µL of the reagent was added, shaken in an orbital shaker protected from light for 10 min and then maintained for 20 min at room temperature with no shaking. Luminescence was recorded on a Biotek Synergy H1 plate-reader, using the green filter set (Excitation: 485/20; Emission: 528/20; DM 510) and 1 s integration time. Statistical significance of differences between groups was calculated using 2-way ANOVA analysis. Differences were concluded significant for p values < 0.05: *p < 0.05, **p < 0.01, ***p < 0.001, ****p < 0.0001. Statistical tests were performed in GraphPad Prism 7.03 (GraphPad Software, CA, USA).

ICP-MS and microscopy studies: MKN-45/HDFa spheroids were generated as above and incubated with AuNR-mPEG@**[4]**$^-$ (0.1 mM) in FBS-free media (50:50 v/v RPMI:DMEM; 100 µL) for 24 h. For ICP-MS, supernatants from two wells were removed and spheroids washed. The spheroids were then immersed in digest solution (HNO_3/HCl = 1:1) with a volume of 5 mL. The dispersions were heated to boiling until complete dissolution. 1 mL of H_2O_2 was then added into the solution, and heating continued until the solution became clear and transparent. The solution was then cooled to room temperature, diluted with 2% HNO_3 to 10 mL, and subsequently analyzed by ICP-MS to determine the concentration of Au and B in each sample. Experiments were performed in duplicate. For optical microscopy analysis, spheroids were washed and fixed overnight at 4 °C in 4% formaldehyde in PBS. Samples were washed in PBS and imaged on an 880LSM Zeiss Confocal microscope using a x20 Plan-Apochromat objective with 0.8 N.A. The sample was viewed using reflection (ex 633 nm), brightfield, and multiphoton (ex 780 nm) microscopy. A 3-pixel averaging filter was

applied as post-processing treatment to multiphoton and reflection images. Where described, z-stacks were taken and maximum intensity images obtained.

For TEM imaging, spheroids were washed and fixed overnight at 4 °C in 2% formaldehyde/2.5% glutaldehyde in Sorensen's buffer (0.1M). Samples were washed with Sorensen's buffer and incubated in OsO_4 diluted to 1% in Sorensen's buffer (1h on ice). After washing, samples were dehydrated in an ethanol series, finishing with pure acetone, and then embedded in Spurr´s embedding medium. Images were acquired with the TEM system described above.

BNCT studies: MKN-45 gastric adenocarcinoma cells were plated with complete media (10% FBS and 1% Penicillin/Streptomycin in RPMI 1640 medium) in T12.5 flasks 24 hours before irradiation to reach 70% of confluency. Cells were maintained in a humid atmosphere at 37 °C and 5% CO_2. One hour before irradiation, AuNR-mPEG@**[4]**$^-$ were added to the cell medium to reach final concentrations of 0.1 or 10 μg/mL in natural boron, corresponding to 5 μM or 500 μM in gold, respectively. Cells were then irradiated (15 min, room temperature) inside the thermal column of the TRIGA Mark II reactor at Pavia University, using a 30 kW reactor power. These conditions correspond to a thermal neutron fluence of 1.30 x 10^{12} cm^{-2}, which is the same order of magnitude expected in clinical BNCT. The irradiation position has been extensively characterized in terms of neutron flux and spectrum as well as background gamma dose by means of activation foils and alanine dosimeters.[49] At a reactor power of 250 kW (maximum condition of operation) the thermal neutron flux is (1.20±0.10) × 10^{10} $cm^{-2}s^{-1}$, while the epithermal and fast components are two and three orders of magnitude lower, respectively. The flux was roughly constant (< 1% variation) along the vertical direction, and thus the flasks were superimposed and irradiated simultaneously.

After irradiation, the medium containing AuNR-mPEG@**[4]**$^-$ was replaced by fresh complete medium. Three hours after irradiation, cells were detached with trypsin EDTA 1x

(Sigma-Aldrich, St. Louis, MO, USA), centrifuged at 1000 rpm for 10 minutes and the pellets resuspended. Samples of the cell suspension (10µL each) and 0.4% Trypan blue solution (10 µL per chamber) were loaded into the chambers of the counting slides. In parallel, control cell samples (not exposed to AuNR-mPEG@**[4]**$^-$) and cell samples mocked-irradiated were processed identically. Cell viability was finally evaluated by means of Trypan blue exclusion assay with LUNA-II automated cell counter (Twin Helix, Italy). All experiments were performed in triplicates.

***In vivo* and *ex vivo* studies**

Animals: All animals were maintained and handled in accordance with the Guidelines for Accommodation and Care of Animals (European Convention for Protection of Vertebrate Animals Used for Experimental and Other Scientific Purposes) and internal guidelines. Experimental procedures were approved by the ethical committee and local authorities. All animals were housed in ventilated cages and fed on standard diet *ad libitum*.

Mouse tumor model development: In order to study the biodistribution of AuNRs in tumor-bearing mice, Rj:NMRI-*Foxn1*$^{nu/nu}$ female mice (7-8 weeks old, Janvier) were subcutaneously inoculated with 2×10^6 MKN-45 tumor cells in the right back. Prior to each inoculation, cells were diluted in sterile PBS:Matrigel (1:1) and mycoplasma test (Lonza) was carried out to ensure that cells were not contaminated. Tumors were measured every 2–3 days with a digital calliper and volumes were calculated as V (mm^3) = [(short diameter)^2 × (long diameter)]/2. Biodistribution studies were carried out when tumor volume was approximately 200–300 mm^3 (~15 days after tumor inoculation).

Biodistribution studies: PET-CT studies with ^{64}Cu-labeled multifunctionalized AuNRs were carried out in MKN-45 tumor-bearing mice (n=4) using an eXplore Vista-CT small animal PET-CT system (GE Healthcare). Anesthesia was induced with 5% isoflurane and maintained by 1.5% to 2% of isoflurane in 100% O_2. For intravenous administration of the

radiotracer, the tail vein was catheterized with a 24-gauge catheter and the labeled NPs (ca. 3–10 MBq) were injected. PET images were analyzed using PMOD image analysis software (PMOD Technologies Ltd, Zürich, Switzerland). Volumes of interest (VOIs) were manually drawn in lungs, liver, heart, kidneys, spleen, brain, stomach, tumor, and bladder using CT images as anatomical reference. VOIs were then transferred to the PET images and time activity curves (decay corrected) were obtained for each organ as cps/cm^3. Curves were transformed into real activity (Bq/cm^3) curves, and injected dose normalization was finally applied to data to get time activity curves as percentage of injected dose per cm^3 of tissue (%ID/cm^3).

***Ex vivo* studies:** Mice were sacrificed at 48 h post injection, after the last imaging session. Organs of interest were collected and weighed, and the radioactivity was measured in a well gamma-counter (Wallach Wizard, PerkinElmer, Waltham, MA, USA). The uptake of ^{64}Cu in the various organs was calculated as a percentage of the injected dose per gram of tissue (%ID/g) according to the prepared standards. The weighed organs were then immersed in digest solution (HNO_3/HCl = 1:1) with a volume of 5 mL. The dispersions were heated to boiling until organs were completely dissolved. 1 mL of H_2O_2 was then added into the solution, and heating continued until the solution became clear and transparent. The solution was then cooled to room temperature, diluted by 2% HNO_3 to 10 mL, and subsequently analyzed by ICP-MS to determine the concentration of Au and B in each sample.

ASSOCIATED CONTENT

Supporting Information. Details for neutron capture calculations, radiochemical stability studies, photothermal characterization of the different nanomaterials and effect of irradiation is aspect ratio and particle core size.

AUTHOR INFORMATION

Corresponding Author

* Jordi Llop. CIC biomaGUNE, Basque Research and Technology Alliance (BRTA), Paseo Miramón 194, 20014 San Sebastián, Guipúzcoa, Spain. Telephone: +34 943 00 5333; e-mail: jllop@cicbiomagune.es

Author Contributions

The manuscript was written through contributions of all authors. All authors have given approval to the final version of the manuscript.

Funding Sources

This work was funded by the Spanish Ministry of Economy and Competitiveness (Projects: CTQ2017-87637-R and MAT2017-86659-R). Part of the work has been performed under the Maria de Maeztu Units of Excellence Program from the Spanish State Research Agency (Grant No. MDM-2017-0720).

REFERENCES

1. Locher, G. L. Biological effects and therapeutic possibilities of neutrons. *American Journal of Roentgenology Radium Therapy and Nuclear Medicine* **1936,** *36* (1), 1-13.

2. Naito, F. Introduction to accelerators for boron neutron capture therapy. *Therapeutic Radiology and Oncology* **2018,** *2*.

3. Kiyanagi, Y.; Sakurai, Y.; Kumada, H.; Tanaka, H. Status of accelerator-based BNCT projects worldwide. *AIP Conference Proceedings* **2019,** *2160* (1), 050012.

4. Bregadze, V. I.; Sivaev, I. B., Polyhedral boron compounds for BNCT. In *Boron Science: New Technologies and Applications*, 2016; pp 181-207.

5. Nakamura, H.; Kirihata, M., Boron compounds: New candidates for boron carriers in BNCT. In *Neutron Capture Therapy: Principles and Applications*, 2012; Vol. 9783642313349, pp 99-116.

6. Yokoyama, K.; Miyatake, S. I.; Kajimoto, Y.; Kawabata, S.; Doi, A.; Yoshida, T.; Asano, T.; Kirihata, M.; Ono, K.; Kuroiwa, T. Pharmacokinetic study of BSH and BPA in simultaneous use for BNCT. *Journal of Neuro-Oncology* **2006,** *78* (3), 227-232.

7. Sauerwein, W. A. G.; Bet, P. M.; Wittig, A., Drugs for BNCT: BSH and BPA. In *Neutron Capture Therapy: Principles and Applications*, 2012; Vol. 9783642313349, pp 117-160.

8. Fang, J.; Nakamura, H.; Maeda, H. The EPR effect: Unique features of tumor blood vessels for drug delivery, factors involved, and limitations and augmentation of the effect. *Advanced Drug Delivery Reviews* **2011,** *63* (3), 136-151.

9. Kueffer, P. J.; Maitz, C. A.; Khan, A. A.; Schuster, S. A.; Shlyakhtina, N. I.; Jalisatgi, S. S.; Brockman, J. D.; Nigg, D. W.; Hawthorne, M. F. Boron neutron capture therapy demonstrated in mice bearing EMT6 tumors following selective delivery of boron by rationally designed liposomes. *Proceedings of the National Academy of Sciences of the United States of America* **2013,** *110* (16), 6512-6517.

10. Maitz, C. A.; Khan, A. A.; Kueffer, P. J.; Brockman, J. D.; Dixson, J.; Jalisatgi, S. S.; Nigg, D. W.; Everett, T. A.; Hawthorne, M. F. Validation and Comparison of the Therapeutic Efficacy of Boron Neutron Capture Therapy Mediated By Boron-Rich Liposomes in Multiple Murine Tumor Models. *Translational Oncology* **2017,** *10* (4), 686-692.

11. Tachikawa, S.; Miyoshi, T.; Koganei, H.; El-Zaria, M. E.; Viñas, C.; Suzuki, M.; Ono, K.; Nakamura, H. Spermidinium closo-dodecaborate-encapsulating liposomes as efficient boron delivery vehicles for neutron capture therapy. *Chemical Communications* **2014,** *50* (82), 12325-12328.

12. Takeuchi, I.; Kishi, N.; Shiokawa, K.; Uchiro, H.; Makino, K. Polyborane encapsulated liposomes prepared using pH gradient and reverse-phase evaporation for boron neutron capture therapy: biodistribution in tumor-bearing mice. *Colloid and Polymer Science* **2018,** *296* (7), 1137-1144.

13. Takeuchi, I.; Tomoda, K.; Matsumoto, K.; Uchiro, H.; Makino, K. PEGylated liposomes prepared with polyborane instead of cholesterol for BNCT: characteristics and biodistribution evaluation. *Colloid and Polymer Science* **2016,** *294* (10), 1679-1685.

14. Yannopoulos, S. N.; Zouganelis, G. D.; Nurmohamed, S.; Smith, J. R.; Bouropoulos, N.; Calabrese, G.; Fatouros, D. G.; Tsibouklis, J. Physisorbed o-carborane onto lyso-phosphatidylcholine-functionalized, single-walled carbon nanotubes: A potential carrier system for the therapeutic delivery of boron. *Nanotechnology* **2010,** *21* (8).

15. Ferreira, T. H.; Miranda, M. C.; Rocha, Z.; Leal, A. S.; Gomes, D. A.; Sousa, E. M. B. An assessment of the potential use of BNNTs for boron neutron capture therapy. *Nanomaterials* **2017,** *7* (4).

16. da Silva, W. M.; Hilário Ferreira, T.; de Morais, C. A.; Soares Leal, A.; Barros Sousa, E. M. Samarium doped boron nitride nanotubes. *Applied Radiation and Isotopes* **2018,** *131*, 30-35.

17. Iizumi, Y.; Okazaki, T.; Zhang, M.; Yuge, R.; Ichihashi, T.; Nakamura, M.; Ikehara, Y.; Iijima, S.; Yudasaka, M. Preparation and functionalization of boron nitride containing carbon nanohorns for boron neutron capture therapy. *Carbon* **2015,** *93*, 595-603.

18. Singh, B.; Kaur, G.; Singh, P.; Singh, K.; Kumar, B.; Vij, A.; Kumar, M.; Bala, R.; Meena, R.; Singh, A.; Thakur, A.; Kumar, A. Nanostructured Boron Nitride with High Water Dispersibility for Boron Neutron Capture Therapy. *Scientific Reports* **2016,** *6*.

19. Tietze, R.; Unterweger, H.; Dürr, S.; Lyer, S.; Canella, L.; Kudejova, P.; Wagner, F. M.; Petry, W.; Taccardi, N.; Alexiou, C. Boron containing magnetic nanoparticles for neutron

capture therapy - an innovative approach for specifically targeting tumors. *Applied Radiation and Isotopes* **2015,** *106*, 151-155.

20. Wang, W.; Lin, J.; Xing, C.; Chai, R.; Abbas, S.; Song, T.; Tang, C.; Huang, Y. Fe_3O_4 nanoparticle-coated boron nitride nanospheres: Synthesis, magnetic property and biocompatibility study. *Ceramics International* **2017,** *43* (8), 6371-6376.

21. Mortensen, M. W.; Björkdahl, O.; Sørensen, P. G.; Hansen, T.; Jensen, M. R.; Gundersen, H. J. G.; Bjørnholm, T. Functionalization and cellular uptake of boron carbide naraoparticles. The first step toward T cell-guided boron neutron capture therapy. *Bioconjugate Chemistry* **2006,** *17* (2), 284-290.

22. Mortensen, M. W.; Sørensen, P. G.; Björkdahl, O.; Jensen, M. R.; Gundersen, H. J. G.; Bjørnholm, T. Preparation and characterization of Boron carbide nanoparticles for use as a novel agent in T cell-guided boron neutron capture therapy. *Applied Radiation and Isotopes* **2006,** *64* (3), 315-324.

23. Grandi, S.; Spinella, A.; Tomasi, C.; Bruni, G.; Fagnoni, M.; Merli, D.; Mustarelli, P.; Guidetti, G. F.; Achilli, C.; Balduini, C. Synthesis and characterisation of functionalized borosilicate nanoparticles for boron neutron capture therapy applications. *Journal of Sol-Gel Science and Technology* **2012,** *64* (2), 358-366.

24. Cioran, A. M.; Teixidor, F.; Krpetić, Ž.; Brust, M.; Viñas, C. Preparation and characterization of Au nanoparticles capped with mercaptocarboranyl clusters. *Dalton Transactions* **2014,** *43* (13), 5054-5061.

25. Pulagam, K. R.; Gona, K. B.; Gómez-Vallejo, V.; Meijer, J.; Zilberfain, C.; Estrela-Lopis, I.; Baz, Z.; Cossío, U.; Llop, J. Gold Nanoparticles as Boron Carriers for Boron Neutron Capture Therapy: Synthesis, Radiolabelling and In Vivo Evaluation. *Molecules* **2019,** *24* (19), 3609.

26. Feiner, I. V. J.; Pulagam, K. R.; Uribe, K. B.; Passannante, R.; Simó, C.; Zamacola, K.; Gómez-Vallejo, V.; Herrero-Álvarez, N.; Cossío, U.; Baz, Z.; Caffarel, M. M.; Lawrie, C. H.; Vugts, D. J.; Rejc, L.; Llop, J. Pre-targeting with ultra-small nanoparticles: boron carbon dots as drug candidates for boron neutron capture therapy. *J Mater Chem B* **2021,** *9* (2), 410-420.

27. Golombek, S. K.; May, J. N.; Theek, B.; Appold, L.; Drude, N.; Kiessling, F.; Lammers, T. Tumor targeting via EPR: Strategies to enhance patient responses. *Advanced Drug Delivery Reviews* **2018,** *130*, 17-38.

28. Man, F.; Lammers, T.; T. M. de Rosales, R. Imaging Nanomedicine-Based Drug Delivery: a Review of Clinical Studies. *Molecular Imaging and Biology* **2018,** *20* (5), 683-695.

29. MacKey, M. A.; Ali, M. R. K.; Austin, L. A.; Near, R. D.; El-Sayed, M. A. The most effective gold nanorod size for plasmonic photothermal therapy: Theory and in vitro experiments. *Journal of Physical Chemistry B* **2014,** *118* (5), 1319-1326.

30. Wang, J.; Dong, B.; Chen, B.; Jiang, Z.; Song, H. Selective photothermal therapy for breast cancer with targeting peptide modified gold nanorods. *Dalton Transactions* **2012,** *41* (36), 11134-11144.

31. Llop, J.; Masalles, C.; Viñas, C.; Teixidor, F.; Sillanpää, R.; Kivekäs, R. The [3,3′-Co(1,2-$C_2B_9H_{11})_2$]-anion as a platform for new materials: Synthesis of its functionalized monosubstituted derivatives incorporating synthons for conducting organic polymers. *Journal of the Chemical Society. Dalton Transactions* **2003,** (4), 556-561.

32. Ali, M. R. K.; Snyder, B.; El-Sayed, M. A. Synthesis and optical properties of small Au nanorods using a seedless growth technique. *Langmuir* **2012,** *28* (25), 9807-9815.

33. Gómez-Graña, S.; Hubert, F.; Testard, F.; Guerrero-Martínez, A.; Grillo, I.; Liz-Marzán, L. M.; Spalla, O. Surfactant (Bi) layers on gold nanorods. *Langmuir* **2012,** *28* (2), 1453-1459.

34. Akiyama, Y.; Mori, T.; Katayama, Y.; Niidome, T. The effects of PEG grafting level and injection dose on gold nanorod biodistribution in the tumor-bearing mice. *Journal of Controlled Release* **2009,** *139* (1), 81-84.

35. Prencipe, G.; Tabakman, S. M.; Welsher, K.; Liu, Z.; Goodwin, A. P.; Zhang, L.; Henry, J.; Dai, H. PEG branched polymer for functionalization of nanomaterials with ultralong blood circulation. *Journal of the American Chemical Society* **2009,** *131* (13), 4783-4787.

36. Wagner, C. D.; Naumkin, A. V.; Kraut-Vass, A.; Allison, J. W.; Powell, C. J.; Rumble, J. R. J., NIST X-ray Photoelectron Spectroscopy Database National Institute of Standards and Technology, Gaithersburg MD, 20899 (2000): NIST Standard Reference Database Number 20.

37. Sóti, Z.; Magill, J.; Dreher, R. Karlsruhe Nuclide Chart – New 10th edition 2018 *EPJ Nuclear Sci. Technol.* **2019,** *5*, 6.

38. Sun, X.; Huang, X.; Yan, X.; Wang, Y.; Guo, J.; Jacobson, O.; Liu, D.; Szajek, L. P.; Zhu, W.; Niu, G.; Kiesewetter, D. O.; Sun, S.; Chen, X. Chelator-free 64Cu-integrated gold nanomaterials for positron emission tomography imaging guided photothermal cancer therapy. *ACS Nano* **2014,** *8* (8), 8438-8446.

39. Tong, X.; Wang, Z.; Sun, X.; Song, J.; Jacobson, O.; Niu, G.; Kiesewetter, D. O.; Chen, X. Size dependent kinetics of gold nanorods in EPR mediated tumor delivery. *Theranostics* **2016,** *6* (12), 2039-2051.

40. Iceta, L. G.; Gómez-Vallejo, V.; Koziorowski, J. M.; Llop, J., Radiochemical stability studies of radiolabelled nanoparticles. In *Isotopes in Nanoparticles: Fundamentals and Applications*, 2016; pp 429-453.

41. Rios, X.; Compte, M.; Gómez-Vallejo, V.; Cossío, U.; Baz, Z.; Morcillo, M. Á.; Ramos-Cabrer, P.; Alvarez-Vallina, L.; Llop, J. Immuno-PET Imaging and Pharmacokinetics of an Anti-CEA scFv-based Trimerbody and Its Monomeric Counterpart in Human Gastric Carcinoma-Bearing Mice. *Molecular Pharmaceutics* **2019,** *16* (3), 1025-1035.

42. Sitarz, R.; Skierucha, M.; Mielko, J.; Offerhaus, G. J. A.; Maciejewski, R.; Polkowski, W. P. Gastric cancer: epidemiology, prevention, classification, and treatment. *Cancer Manag Res* **2018,** *10*, 239-248.

43. Lu, S.; Xia, D.; Huang, G.; Jing, H.; Wang, Y.; Gu, H. Concentration effect of gold nanoparticles on proliferation of keratinocytes. *Colloids and Surfaces B: Biointerfaces* **2010,** *81* (2), 406-411.

44. Mahmoud, N. N.; Al-Kharabsheh, L. M.; Khalil, E. A.; Abu-Dahab, R. Interaction of Gold Nanorods with Human Dermal Fibroblasts: Cytotoxicity, Cellular Uptake, and Wound Healing. *Nanomaterials (Basel)* **2019,** *9* (8), 1131.

45. Heidari, Z.; Salouti, M.; Sariri, R. Breast cancer photothermal therapy based on gold nanorods targeted by covalently-coupled bombesin peptide. *Nanotechnology* **2015,** *26* (19).

46. Zhang, Y.; Yin, L.; Xia, X.; Hu, F.; Liu, Q.; Qin, C.; Lan, X. Synthesis and bioevaluation of Iodine-131 directly labeled cyclic RGD-PEGylated gold nanorods for tumor-targeted imaging. *Contrast Media and Molecular Imaging* **2017,** *2017*.

47. Costa, E. C.; Moreira, A. F.; de Melo-Diogo, D.; Gaspar, V. M.; Carvalho, M. P.; Correia, I. J. 3D tumor spheroids: an overview on the tools and techniques used for their analysis. *Biotechnology Advances* **2016,** *34* (8), 1427-1441.

48. Kume, M.; Carey, P. C.; Gaehle, G.; Madrid, E.; Voller, T.; Margenau, W.; Welch, M. J.; Lapi, S. E. A semi-automated system for the routine production of copper-64. *Applied Radiation and Isotopes* **2012,** *70* (8), 1803-1806.

49. Bortolussi, S.; Protti, N.; Ferrari, M.; Postuma, I.; Fatemi, S.; Prata, M.; Ballarini, F.; Carante, M. P.; Farias, R.; González, S. J.; Marrale, M.; Gallo, S.; Bartolotta, A.; Iacoviello, G.; Nigg, D.; Altieri, S. Neutron flux and gamma dose measurement in the BNCT irradiation facility at the TRIGA reactor of the University of Pavia. *Nuclear Instruments and Methods in Physics Research Section B: Beam Interactions with Materials and Atoms* **2018,** *414*, 113-120.